PHYSICAL REVIEW A, VOLUME 62, 033202

Angular-resolved studies of fragmentation in fullerene-fullerene collisions

A. V. Glotov and E. E. B. Campbell*

Department of Experimental Physics, Göteborg University and Chalmers University of Technology, SE-41296 Göteborg, Sweden

(Received 28 January 2000; published 10 August 2000)

Fragmentation channels in collisions between fullerenes were studied as a function of collision energy (115–1400 eV center of mass) and scattering angle using a rotatable reflectron time-of-flight mass spectrometer. The products from fusion reactions and those from inelastically scattered (but not fused) projectile ions represent the two fragmentation channels in the collisions studied. The fragment size dependence is discussed as a function of collision energy and scattering angle. The results are in good qualitative agreement with theoretical models. A change in fragmentation behavior due to the onset of a finite-system analog of a phase transition in the reaction products can be seen in the mass and angular distributions of the fragment ions.

PACS number(s): 36.40.−c

I. INTRODUCTION

In recent years there has been increasing interest in the study of collisional interactions between atomic clusters. The behavior of such processes is governed by the dynamics of systems with a large yet finite number of degrees of freedom and also has analogies to the physics of colliding atomic nuclei and liquid droplets [1]. In particular, the observation of effects such as deep inelastic scattering, fusion, and multifragmentation [2–6] can be closely related to the dynamics of collisions between atomic nuclei [7].

Collisions between fullerenes are the most studied systems [2–4,9–29] and have proved a very convenient model for such research. Fullerenes are covalently bound atomic clusters with a hollow cage structure [8] and therefore cannot be regarded as ''typical'' atomic clusters due to their unique geometry. Their highly directional covalent bonding does lead to some significant differences in collisional behavior compared to calculations of metal cluster-cluster collisions or collisions between atomic nuclei. This is particularly apparent in the fusion reaction cross sections [2,3,10]. However, there are still many similarities in behavior and, since fullerenes are the only systems that are experimentally available for detailed investigations, they have been the most widely studied.

Investigations of cluster-cluster collisions involving fullerenes have included charge-transfer studies [21,26–29] and very high energy fragmentation investigations [12]. As well as the study of charge-transfer collisions [26–28], the main interest of our group has been the study of fusion and fragmentation reactions at low to intermediate collision energies of 60–200 eV [in the center-of-mass (CM) frame] [2,4,9–11]. In this energy range, fusion was found experimentally to be a significant reaction channel in agreement with MD [13,16,17,23,24] and QMD calculations [3]. The experimentally determined energetic threshold for fusion and the increase of the fusion cross section in the low kinetic energy region close to threshold can be easily understood in terms of a simple phenomenological absorbing sphere model [2]. In the range of moderate kinetic energies (>150 eV), the fusion cross section decreases much more rapidly than predicted by the simple model [11]. This has been attributed to a change in fragmentation behavior due to the onset of a finite-system analog of a phase transition in the fusion product [11]. Below this energy, the fragmentation can be described as predominantly occurring via successive loss (evaporation) of C_2 units. This does not deflect the fusion product sufficiently out of the beam path to entirely avoid detection, although, as we will discuss later, there is likely to be some loss of signal [all the experiments reported up until now have been at a laboratory detection angle of $(0 \pm 0.6°)$]. The more drastic decrease and disappearance of the fusion signal reported at the higher kinetic energies around 200 eV [2,10] were interpreted as indicating the rapid loss of the fullerene structure after collision and the onset of a multifragmentation behavior leading to the production of a number of large fragments, one of which carries the positive charge. These fragments would be expected to be scattered in a larger angular range and thus avoid detection. The work reported in this paper improves on our previous measurements and, in particular, extends the measurements to the determination of the angular dependence of the fragmentation. These measurements allow a much greater insight into the dynamics of the fullerene-fullerene collisions in the interesting collision energy range where fusion is a significant reaction channel. The measurements reported cover a collision energy range from 115 eV up to 1400 eV and a laboratory scattering angle range up to 12°. We confirm the picture inferred from our earlier work and clearly show that the rapid decrease in the fusion cross section reported earlier is due to an abrupt change in the fragmentation mechanism related to the onset of a ''phase transition.''

II. EXPERIMENTAL SETUP

The experimental setup for the measurement of mass spectra as a function of both detection angle θ and collision energy E is a modification of the apparatus we have used previously to study fusion reactions between fullerenes and has been described in detail before [2]. Therefore, we only briefly describe the main modifications for the current experiments here. A schematic diagram of the apparatus is shown in Fig. 1. The pulsed beam of projectile ions ($C_{60}{}^{+}$ in our experiments) is formed and mass-selected in the usual

---

*Author to whom correspondence should be addressed. FAX: +46 31 772 3496. Email address: Eleanor.Campbell@fy.chalmers.se

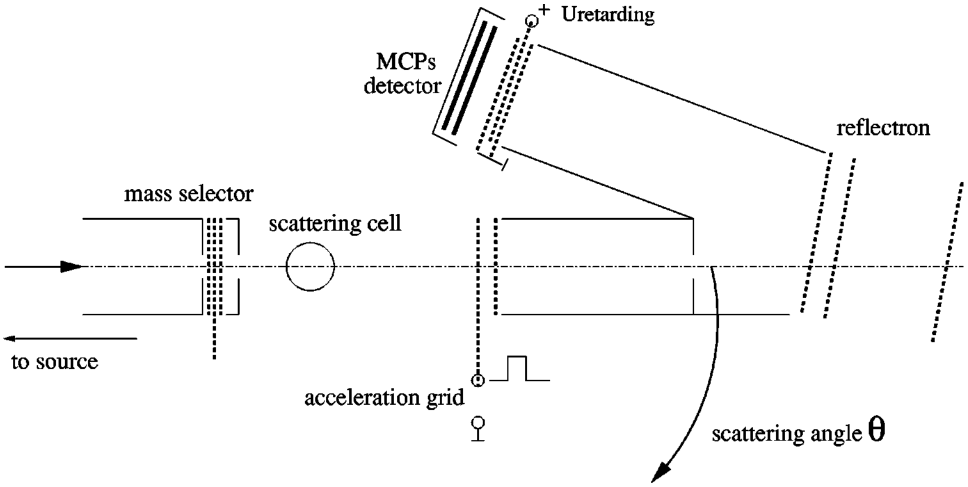

FIG. 1. Schematic view of the reaction-detection part of the experimental setup.

way as described before [2] and directed into the scattering cell. The scattering cell is a cylindrical oven with a circular entrance of 2 mm diameter and a horizontal exit slit of 2 mm height allowing the detection of scattered ions at laboratory angles up to 80°. Fullerene powder of high purity ($\geqslant 99.4\%$ C_{60}) is evaporated inside the cell forming the target gas. Single collision conditions are ensured by keeping the temperature of the scattering cell in the region of 450–500°C [2]. The temperature of the oven is monitored by a thermocouple.

Projectile and product ions exiting the scattering cell are detected by a reflectron time-of-flight mass spectrometer coupled with a multichannel plate detector. The reflectron together with the ion detector can be rotated in the horizontal plane thus scanning the scattering angles. The kinetic energy of the detected ions can be analyzed by applying a positive potential on the grid in the front of the detector. The angular resolution of the apparatus is $(\pm 0.6)^\circ$ and similar to the resolution of the previous experiments carried out at a scattering angle of 0° [2]. The apparatus resolution is predominantly defined by an aperture placed in front of the first grid of the reflectron (see Fig. 1). Because of the very low product intensity, a digital multichannel scaler is coupled to a discriminator for data acquisition in a single ion counting mode. The angular spread of the parent ion beam was measured to be $(2\pm 0.5)^\circ$ [full width at half maximum (FWHM)] with an energy spread (FWHM) of 5% of the laboratory collision energy.

In order to increase the detection efficiency of low mass ions with different velocities and thus to clearly identify the source of the fragments, i.e., whether they arise from inelastically scattered $C_{60}{}^+$ or the fusion product, an additional acceleration unit was added to the apparatus. Two grids were placed at a distance of 60 mm from the center of the scattering cell with 10 mm distance between them. The second grid was set at zero potential and a positive pulsed potential (higher than the initial projectile energy) was applied to the first grid. The timing of the pulsed field could be adjusted to detect ions within a defined velocity range. A distance of 10 mm between the grids proved to be a good compromise choice allowing the resolution of ions of the same mass but velocities differing by 5–10% (depending on the mass).

In the experiments using the above acceleration unit, the acceptance angle is a dynamically changing quantity depending on the scattering angle, the ion velocity and mass, and the value of the acceleration field. This configuration is thus not particularly well suited for the determination of angular distributions but it still gives a useful overall picture of the scattering behavior.

III. RESULTS

In the present experiments we have studied collisions between $C_{60}{}^+$ and C_{60} in the range of center-of-mass kinetic energies from 115 eV (fusion region) up to 1400 eV and scattering angles from 0° up to 12°. We prefer to give the collision energies in the center-of-mass reference frame (in our case simply half of the laboratory collision energy) since, first, this is the amount of energy available for conversion to internal energy of the collision products and, second, for consistency since we have always referred to the center-of-mass energies in our previous papers. We will, however, report the scattering angles in the laboratory frame of reference. As will be seen below, there are many different possible reaction channels with a large range of product sizes and inelasticities ranging from zero up to the entire center-of-mass energy. It is thus extremely difficult to clearly separate the different contributions. This makes a reliable conversion from the laboratory to center-of-mass scattering angle practically impossible.

Typical time-of-flight mass spectra for different scattering angles are shown in Fig. 2. The kinetic energy for the primary $C_{60}{}^+$ projectiles for this experiment was (1000 ± 50) eV (500 eV center-of-mass collision energy), well beyond the energy range where fusion was observed in the earlier experiments [2]. For zero scattering angle, the mass spectra are dominated by the $C_{60}{}^+$ primary peak around 115 μs. There are also low-intensity (two to three orders of magnitude smaller) sharp peaks sitting on a broad structureless background in the region of $102-113$ μs. The two peaks directly in front of the primary ion peak arise from metastable fragmentation of the hot primary ions beyond the

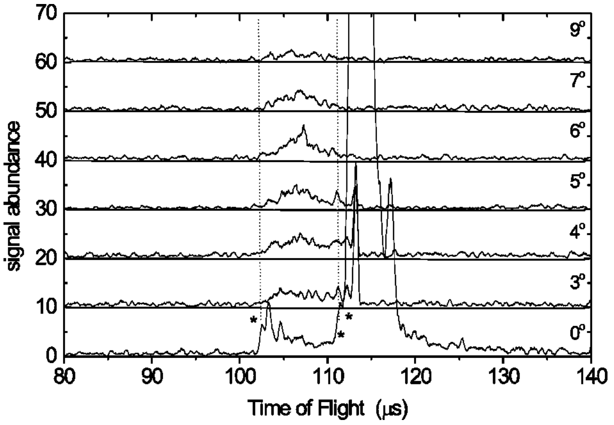

FIG. 2. Time-of-flight spectra for different scattering angles. Collision energy 500 eV. * : signals due to collisions with reflectron grid and metastable fragmentation of primary ions.

mass selector. They correspond to the two fragments $C_{56}{}^{+}$ and $C_{58}{}^{+}$. The peak at lower flight times is an experimental artifact and arises due to fragmentation of primary $C_{60}{}^{+}$ on the grid inside the reflectron. Its intensity is proportional to the primary ion signal. With increasing scattering angle the intensity of the primary $C_{60}{}^{+}$ signal drops as well as the signal due to collisions with the reflectron grid and metastable fragmentation of the primary ions.

For scattering angles between 3° and 9°, a broad signal due to fragments can be clearly detected at flight times 102–113 μs. It reaches its maximum value at about 6°. The signal drops below the noise level for scattering angles higher than 10°. The arrival time-of-flight window for the fragment signal is practically independent of scattering angle, indicating that there is no major change in the mass range of the detected fragments as the angle is increased although the intensity distribution may shift somewhat.

Integrated signal intensities are plotted in Fig. 3 as a function of laboratory scattering angle for the same collision energy. Here we plot both the fragmentation intensity, obtained by integrating over the fragment distributions in the time-of-flight spectra for each scattering angle, and the intensity of elastically scattered projectile ions. The angular distribution of the parent ion beam (in the absence of target gas) is shown for comparison. The behavior of the elastically scattered primary $C_{60}{}^{+}$ ions will be discussed in a separate paper [30] and is just shown here for completeness. The angular distribution of the fragment ions is considerably broader than the elastically scattered primary ions with a maximum intensity at a detection angle of approximately 5°. A clear signal is detectable up to an angle of about 10°. Beyond this, it is not possible to distinguish any scattering signal from the noise level.

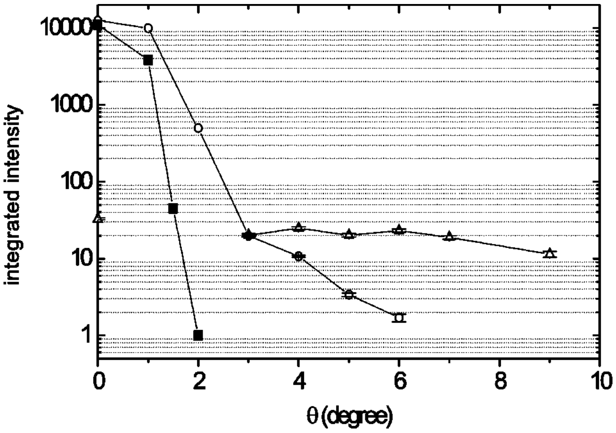

FIG. 3. Integrated signal intensity for different ions, collision energy 500 eV. Not scattered primary ions signal profile (squares), elastically scattered primary ions signal profile (open circles), projectile fragments (open triangles).

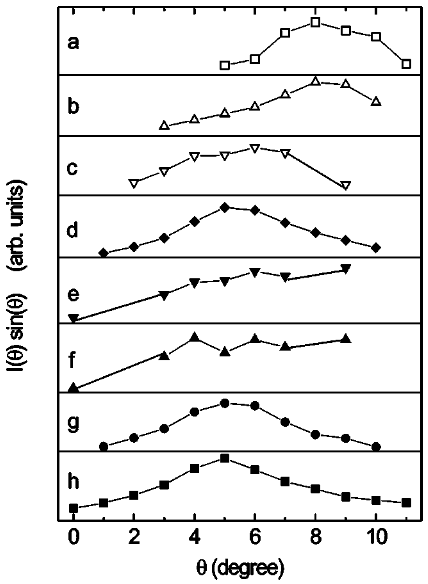

FIG. 4. Integrated fragment intensities for different collision energies as a function of laboratory scattering angle θ. (a) 131 eV, (b)160 eV, (c) 285 eV, (d) 500 eV, (e) 750 eV, (f) 860 eV, (g) 1200 eV, (h) 1380 eV.

Similar behavior is seen over the entire range of collision energies investigated. Some examples are shown in Fig. 4. At the lowest collision energies the distribution has a clear maximum (at 8° for 165 eV decreasing to 6° as the collision energy increases to 500 eV). The distribution is rather narrow for 165 eV (3°–4° FWHM) and increases with increasing collision energy. For intermediate collision energies (665–860 eV) no maximum is observed in the angular range covered and the signal appears to be still increasing beyond 10°. Beyond center-of-mass energies of 1 keV the distribution again shows a maximum at an angle of 5° and a FWHM in the range 4°–5°.

The time of flight at which an ion signal is detected depends both on the mass of the ion and its velocity. The broad signals shown in Fig. 2 thus cannot be identified with particular fragment sizes without further information. As described in detail previously [2], we have the possibility to measure the kinetic energy distribution of the detected ions by using a retarding field analyzer. From the knowledge of the geometry of the experimental setup and the kinetic energy of the primary and product ions, we can calculate the expected flight times for ions of different masses and compare them with the experimental time-of-flight data. Thus we

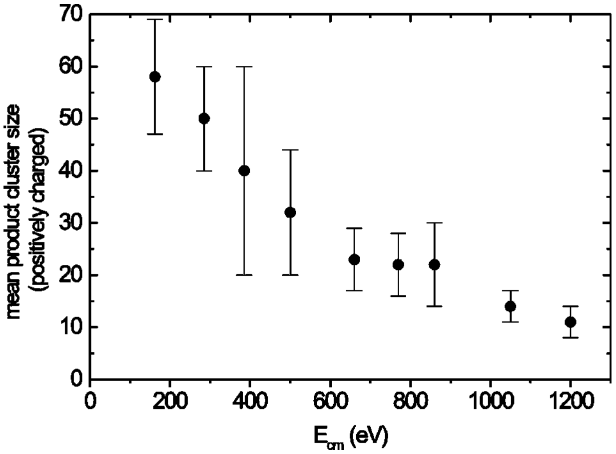

FIG. 5. Mean product cluster size as a function of collision energy. The bars show the range of detected masses.

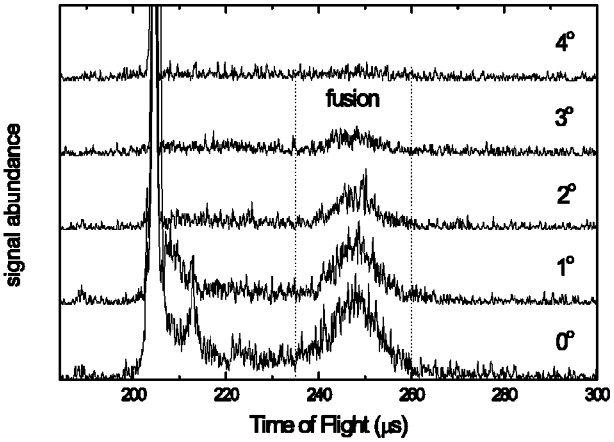

FIG. 6. Time-of-flight spectra for collision energy 131 eV for different laboratory scattering angles θ.

can determine the distribution of fragment masses corresponding to the detected signal. Such an analysis shows that the fragment signals seen in Fig. 2 and used to calculate the angular distributions shown in Fig. 4 can only be attributed to fragment ions with relatively high velocities (75–95% of the velocity of the primary ions) and masses lower than the projectile ion mass of 60 carbon atoms. These fragments are therefore the result of fragmentation of primary C_{60}^+ excited in inelastic collisions and do not have their origin in a short-lived fusion complex.

The above analysis also allows us to determine the dependence of the fragment mass distribution on collision energy. That this changes noticeably with collision energy (in contrast to the angular distributions with the possible exception of the intermediate energies) can be clearly seen in Fig. 5. Here we have plotted the average fragment size after correcting the data for the velocity-dependent detection efficiency [2]. The bars on the symbols do not indicate error bars but show the range of detected masses. The intermediate energy range, which shows a broader angular distribution, is also the energy range where the fragment mass distribution is clearly bimodal. This will be discussed further in the following section.

Ions from a fused collision product can be clearly seen at lower collision energies. An example of the scattering angle dependence of the ion signal for a collision energy of 115 eV is shown in Fig. 6. The large broad signal, arriving at times considerably longer than the projectile ions, is due to the products of a fusion reaction. The dashed lines indicate the position of ions of mass 1440 u (C_{120}^+) and 1080 u (C_{90}). There is only a slight shift of the intensity distribution of the signal towards lower flight times (smaller fragments) with increasing angle with a cutoff at about 4°. At this collision energy there is practically no fragmentation observed from inelastically scattered projectiles.

The detection efficiency for small ($n<30$) fragment ions from a fused product is rather low in the above experiments since they have very low energies and it is possible that some do not complete their trajectory through the reflectron to be detected on the channel plates. In addition, depending on the collision energy, the small fragments can arrive very close to the position of the projectile ion signal making an unambiguous identification difficult. For this reason it is necessary to use the post-acceleration unit, described above, to determine whether any fusion products, corresponding to small carbon fragment ions ($n<30$), are present at high collision energies.

Typical time-of-flight mass spectra for a collision energy of 155 eV and a scattering angle of zero degrees are shown in Fig. 7 for different delay times before the post-acceleration field is switched on. The time is measured with respect to the initial extraction pulse for the projectile ion beam. The time-of-flight spectrum measured for $\delta t=\infty$, i.e., when no post-acceleration field is switched on, is identical to

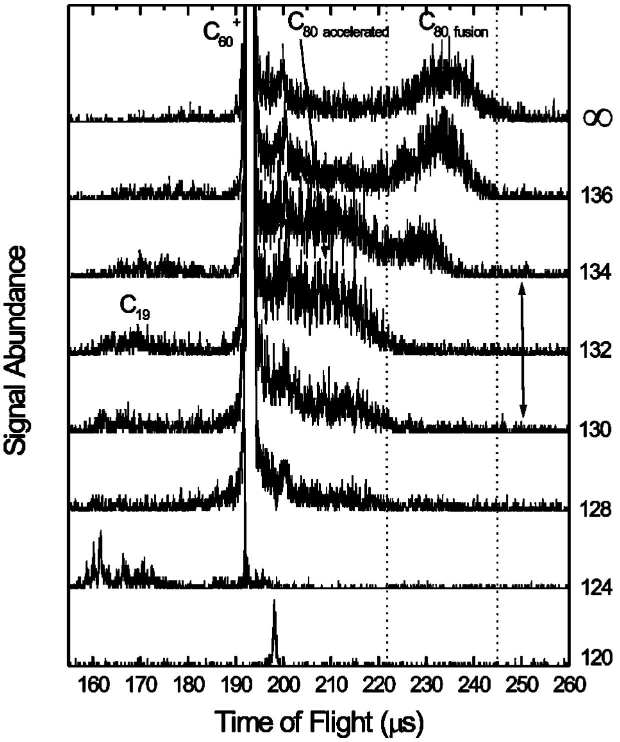

FIG. 7. Time-of-flight mass spectra for collision energy 155 eV, recorded at zero scattering angle for different post-acceleration delay times.

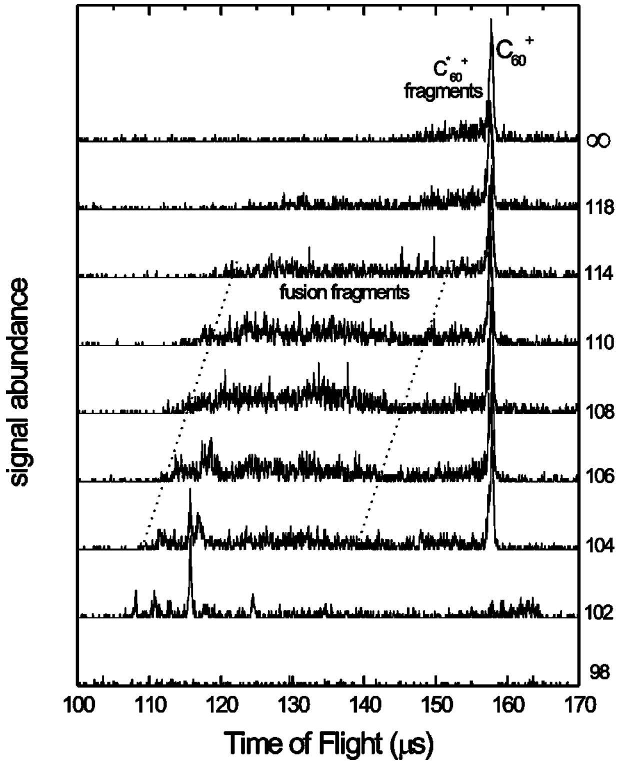

FIG. 8. Time-of-flight mass spectra for collision energy 240 eV, recorded at zero scattering angle for different acceleration times.

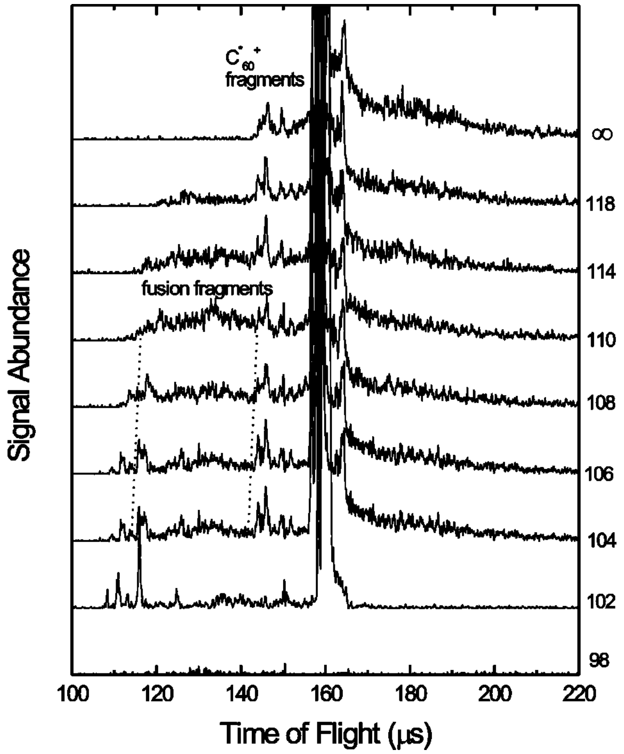

FIG. 9. Time-of-flight mass spectra for collision energy 240 eV, recorded at 3° scattering angle for different acceleration times.

the one measured under normal circumstances. The peak from $C_{60}{}^{+}$ primary ions dominates the spectrum and shows the typical tail to longer flight times. The fusion signal is observed at 222–245 μs and the maximum of the distribution corresponds to the $C_{80}{}^{+}$ fusion fragment. When a positive pulsed field (in this case 400 V) is applied to the first grid of the acceleration unit, as described earlier, then at very short delay times no ion can pass through the potential barrier made by the first acceleration grid and no signal is detected. At approximately $\delta t = 120$ μs the accelerated primary ion signal is detected (peak at approximately 198 μs). This arrives at later times than normal although it has been additionally accelerated because the ions can penetrate further into the reflectron and thus travel a longer distance before detection. At $\delta t = 128$ μs, the primary signal has gained its original shape indicating that all ions with the velocity of the primary ion beam have passed through the acceleration unit before it has been switched on and are therefore not accelerated. The time-of-flight spectrum fully gained its original shape including the fusion signal at $\delta t = 136$ μs, indicating that all product ions have passed the acceleration unit by this time. There is a short time window between $\delta t = 130$–134 μs, as shown by an arrow in Fig. 7, where fusion products were accelerated. This is exactly the time window we expect assuming that the velocity of the fusion compound is half that of the projectile ions. It can also be seen that this signal has split into two parts (also indicated by arrows from the top): the main part is around 210 μs, unfortunately partially masked by the tail of the primary signal but still visible. These are the same ions as the broad peak observed at around 235μs, corresponding to a mass distribution centered about $C_{80}{}^{+}$, without the extra acceleration. The second, smaller part that appears at 160–175μs corresponds to fragment ions with a velocity close to half of the initial projectile ion velocity (indicating completely inelastic, fusion collisions) and a mass distribution centered around $C_{19}{}^{+}$.

A second example at a higher collision energy of 240 eV where no fusion signal was detected in the earlier experiments [2] is shown in Fig. 8. It shows all the above mentioned features except there is no clear, broad signal from fusion products at flight times longer than the projectile ions in the absence of the acceleration field. Again, the spectra are dominated by the primary $C_{60}{}^{+}$ signal with a flight time of 158 μs, without additional acceleration. The signal from fragmented projectile ions is observed at 145–155 μs. On increasing the delay time of the acceleration field, the spectrum gains it original shape at $\delta t = 118$ μs. When δt is between 104 and 110 μs, an additional signal is detected (shown between sloped dashed lines) which changes somewhat in size and shape as the delay time is changed, shifting towards longer flight times as the delay increases. It disappears again for longer delay times. Analysis of the flight times and delay times shows that this signal must be due to small fragments ($n < 30$) from a fused product. These ions could not be detected in earlier experiments since they were completely masked by the long tail on the projectile ions (and also due to the problem of detection efficiency, discussed above).

The same experiment is shown in Fig. 9 for a scattering angle of 3°. Although the noncollided projectile ions are no longer detectable at this scattering angle, there is still a small

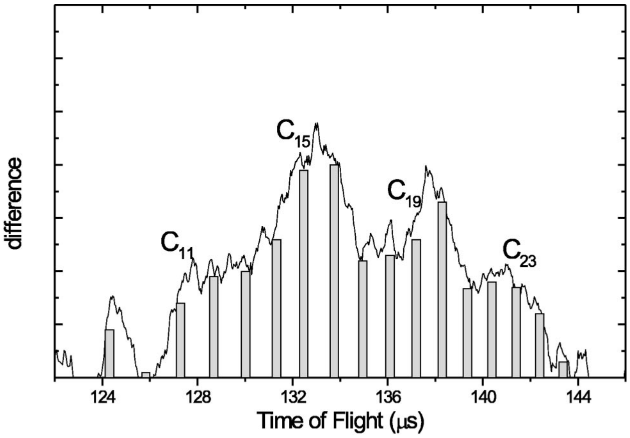

FIG. 10. Collision energy 240 eV, same experiment as in Figs. 8 and 9, post-acceleration delay 108 μs. Difference between time-of-flight spectra recorded with room-temperature scattering cell (no collisions) and with heated scattering cell (collisions). The bars show the calculated times of flight for small clusters at this post-acceleration delay time.

$C_{60}{}^{+}$ signal due to scattered projectile ions. The dependence of the mass spectra on delay time is essentially the same as for zero scattering angle but the signal from both fragmented inelastically collided projectiles and from a fused compound is more pronounced compared to the previous spectra since the large background signal from the intense projectile ion peak is missing. The signal from the fusion fragments is similar in form to that recorded at 0° and there is no indication of a significant change in fragment mass distribution with increasing scattering angle.

Unfortunately, the experiments have shown that a significant part of the signal with flight times corresponding to accelerated fusion products also contains signals from background gas, also observable under conditions in which no collisions between fullerenes can take place (cold scattering cell). In order to better analyze the fragment distribution coming from a fused compound and to remove the artifact signal, we have recorded the spectra with and without the presence of target fullerenes and subtracted one from another. An example of such a difference spectrum is shown in Fig. 10. The experimental data are compared with calculated flight times for fragment ions assuming they are produced with a velocity equal to half the projectile ion velocity. Although the individual mass peaks are not resolved, the experimental data clearly show the ‘‘magic number’’ structure well known for small carbon cations with maxima at $n=7$, 11, 15, 19, and 23. The agreement between the simulated flight times and the structure in the experimental data is very good over the entire delay range where the fusion products can be detected.

IV. DISCUSSION

From a first consideration of the experimental data it is clear that there are two main channels for fragment formation in our experiment:

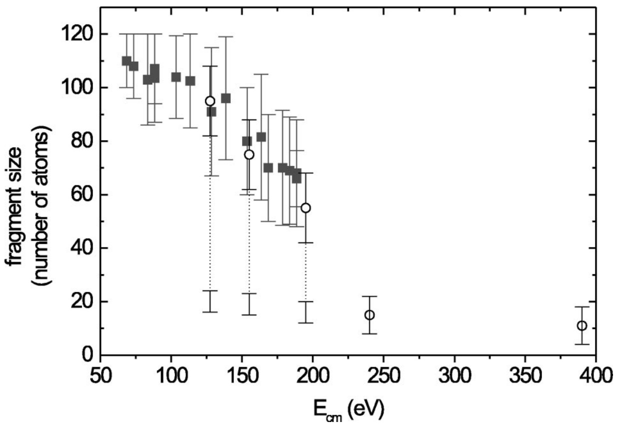

FIG. 11. Average fragment size of products of earlier experiments at 0° detector angle [2] (squares) and data from post-acceleration experiments (open circles) plotted as a function of collision energy. The bars indicate the range of detected masses.

$$\begin{tikzcd}
 & \mathrm{C}_{60}+\mathrm{C}_{60}^{+*} \arrow[dr] & \\
\mathrm{C}_{60}+\mathrm{C}_{60}^{+} \arrow[ur] \arrow[dr] & & \mathrm{C}_{\mathrm{n}}^{+}(\mathrm{v}'\leq \mathrm{v}_{\mathrm{p}})+\mathrm{kC}_{\mathrm{m}} \\
 & \mathrm{C}_{120}^{+*} \arrow[dr] & \\
 & & \mathrm{C}_{\mathrm{n}}^{+}(\mathrm{v}'\approx 0.5\mathrm{v}_{\mathrm{p}})+\mathrm{kC}_{\mathrm{m}}
\end{tikzcd}$$

where v_p is the velocity of projectile ions, v' is the velocity of the product ions after fragmentation, and n,k,m are the number of atoms in the fragmented fullerenes. Here the upper channel indicates inelastic scattering of the projectile ion with subsequent fragmentation. The velocity of the fragment in this case is somewhat less than the velocity of the projectile, depending on the degree of inelasticity plus a contribution from the kinetic energy released in the fragmentation. The lower channel indicates the fusion reaction with the formation of the highly excited compound cluster and subsequent fragmentation. In this case, the velocity of the fragment ions will be half the projectile velocity in the laboratory frame (zero in the center-of-mass frame) plus the kinetic energy released in the fragmentation process. In the following we will discuss these two processes in more detail and provide some explanations for the dependence of the observed mass and angular distributions on collision energy.

A. Fusion products

The situation with regard to the products from fusion reactions is somewhat simpler than the situation for inelastic scattering since we know that the collisions have to be completely inelastic. The dependence of the fragment size distribution from the fusion reaction is plotted as a function of collision energy in Fig. 11. The symbol gives the average fragment size with the bars indicating the range of the mass distribution. Two bars plotted for the same collision energy indicate that the mass distribution is bimodal. For compari-

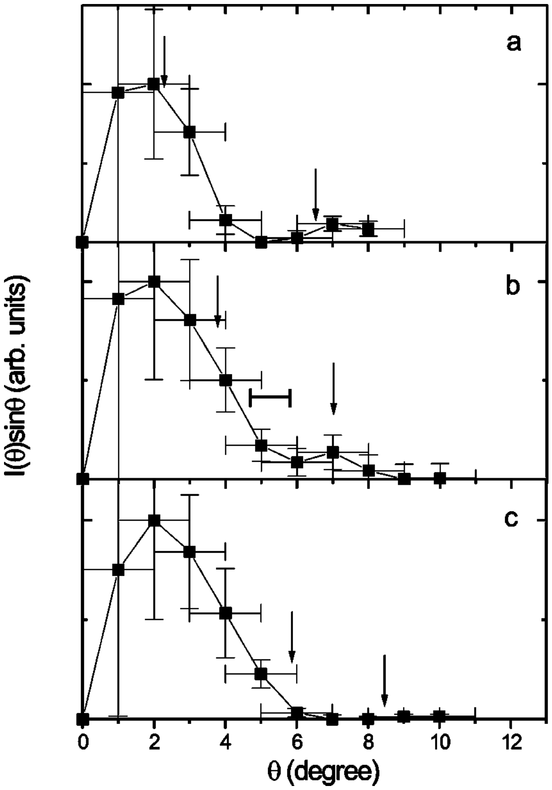

FIG. 12. Integrated fusion signal intensity $[I(\theta)\sin\theta]$ plotted as a function of scattering angle. Collision energies of (a) 122 eV, (b) 131 eV, (c) 165 eV. Intensities have been normalized to the same maximum value. The arrows indicate the estimated maximum scattering angle for the maximum and minimum sized fullerenelike fragments detected in the experiment. The horizontal bar indicates the estimated maximum scattering angle range for the small fragments detected at this collision energy.

son we have plotted the earlier data from [2]. In these earlier experiments it was not possible to observe the small ($n < 30$) fragments which we can now see but in very low intensity for a collision energy of 130 eV. This is exactly the collision energy where the earlier experiments showed the beginning of an abrupt decrease in the magnitude of the fusion cross section. The onset of a bimodal fragment distribution in experiments in which C_{60} is excited, either in collisions or by photon absorption, has been shown, with the help of a simple statistical maximum entropy model, to be related to the onset of a ''phase transition'' in the fullerene that occurs for an excitation energy of around 85 eV [31]. Similar behavior is expected for the $C_{120}{}^{+}$ fusion compound but at a higher excitation energy in the range 150–200 eV [4]. If the internal energy in our projectile ions is taken into consideration (~ 25 eV), this range is in excellent agreement with the observed onset of the bimodal distribution on Fig. 11. The new experiments are thus a very nice confirmation of our interpretation of the abrupt drop in the fusion cross section discussed in [2].

The angular dependence of the integrated intensity of fragment ions from a fusion reaction is shown in Fig. 12 for collision energies of 115 eV to 165 eV. The distributions are concentrated more at small angles than those measured for fragmentation from inelastically scattered projectile ions (Fig. 4). We do not give angular distributions for higher collision energies here since this requires the post-acceleration unit to be sure of detecting the small fragments and such measurements have poorer angular resolution.

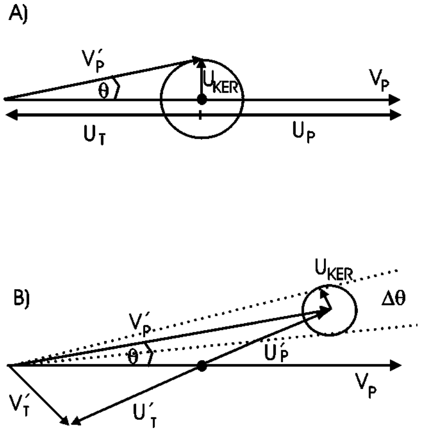

FIG. 13. Newton diagram for $C_{60}{}^{+}+C_{60}$ collision for (a) fusion reaction and (b) inelastic scattering. Here v is velocity in the lab system, u is velocity in the center-of-mass system, p is the projectile, t is the target, and u_{KER} is velocity due to kinetic energy release of a fragment.

Assuming that the fusion compound formed in the collision undergoes a very rapid energy equilibration (shown by QMD calculations in [3]) and then undergoes a completely statistical fragmentation, we can estimate the expected cutoff angle as a function of collision energy. A Newton diagram for the collisions is shown in the upper part of Fig. 13. Immediately after collision, the velocity of the fusion compound in the center-of-mass reference frame will be zero. The final center-of-mass velocity of the fragment ions (u_{KER}) will be given by the accumulated kinetic energy released in the fragmentation process. This will be randomly distributed in space. The maximum detectable laboratory scattering angle ($\theta_{\max}$) is thus determined by the magnitude of the kinetic energy release which, in turn, depends on the temperature of the fused compound and the mass of the fragment. We assume that the small fragments ($n < 30$) are produced by a multifragmentation process in which the highly excited fusion compound disintegrates into a number of ring and chain fragments, one of which carries the positive charge and is detected in the experiment [4,11]. This may undergo a further evaporative step by emitting a C_3 molecule. The large fullerenelike fragments are assumed to be produced by successive evaporative loss of C_2 molecules [2]. Obviously, this is an oversimplification—the small fragments may undergo further evaporative cooling and the large fragments may well be produced with the loss of neutral fragments larger than C_2, especially at such high excitation energies. However, for a first approximation, these seem to be reasonable assumptions. In order to obtain an estimate of the temperature of the fragments, we make use of the maximum entropy calculations presented in [4] which give the relationship between total internal energy and fragment temperature, reproduced here in Fig. 14. These calculations extend those for C_{60}, reported in [31], by making some simple assumptions con-

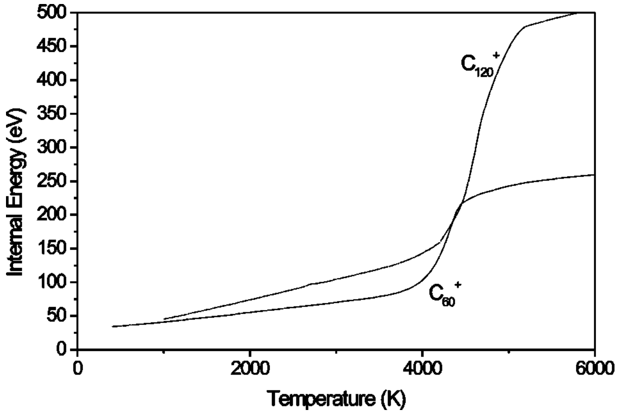

FIG. 14. Average excitation energy as a function of fragment temperature as estimated by a maximum entropy model for C_{60}^+ and C_{120}^+ [4,31].

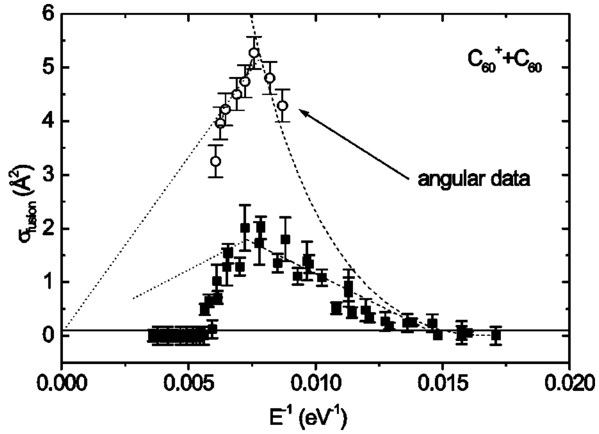

FIG. 15. Experimentally measured fusion cross section for $C_{60}^+ + C_{60} \rightarrow C_{120}^{+}*$ collisions as a function of collision energy^{-1} reported in [2] for a detection angle of $(0 \pm 0.6)°$ (squares) and from scattering angle integration experiments (circles).

cerning the binding energies and ionization potentials of the larger fullerene species based on the expression given by [32]. Further work on applying the maximum entropy formalism to the fragmentation of C_{120} taking the possible role of different isomeric species better into account and comparing mass distributions with experimental results is in progress.

We can estimate the maximum detectable scattering angle for the different collision energies. The total internal energy immediately after collision is given by the initial internal energy of the projectile and target ($\sim$25 eV) plus the center-of-mass collision energy. From Fig. 14 we can relate this total internal energy to a fragment temperature. We assume that the kinetic energy, $\epsilon = kT$, is released in each fragmentation step and for multiple fragmentation we estimate the net velocity after the chain of fragmentation, considering it to be a ''random walk'' process, to be $\sqrt{N}v'$, where N is the number of fragmentation steps and v' is the average velocity gained by a fragment ion in a single fragmentation. Assuming successive C_2 loss, this leads to the maximum possible laboratory scattering angles indicated by the vertical arrows in Fig. 4 for the maximum and minimum sized fullerenelike fragments detected at this collision energy. The emission of larger fragments would lead to a decrease in the maximum observable angle, mainly due to the decrease in N. The simple estimate gives rather good agreement with the experimental measurements. We also see that as the collision energy increases, the assumption of entirely C_2 fragmentation steps probably breaks down since the maximum laboratory angle is overestimated in this case. We can carry out a similar estimate for the small fragment ions although they are of low intensity for these collision energies and do not contribute significantly to the overall scattering intensity. The horizontal bar in Fig. 12(b) indicates the range of maximum scattering angles at this collision energy for the observed mass range $n = 15$–23.

It is obvious from considering Fig. 12 that the earlier measurements of the fusion cross section, at a scattering angle of $0° \pm 0.6°$, considerably underestimated the value of the cross section, even at an energy of 130 eV (close to the maximum of the reported cross section), since many of the scattered fragments went undetected. From our present measurements we can estimate the corrected value of the cross section and the behavior of the fusion cross section as the collision energy is increased. This is plotted in Fig. 15. The cross section is now seen to be much higher (although still considerably lower than the geometrical cross section due to the steric effects discussed in earlier papers [2,10,11]). It also appears as if there might be a less extreme drop in the cross section at high energies after the onset of the ''phase transition'' when the scattered fragments are considered, although more data points are needed to be sure. This would give better agreement with the simple phenomenological absorbing sphere model used to describe the fusion reaction if it proved to be the case (dashed line in Fig. 15).

B. Fragmentation after inelastic scattering

The angular distributions shown in Fig. 4 show an interesting trend with increasing collision energy. The distribution is centered around a laboratory scattering angle of about 8° for the lowest collision energy investigated. It then broadens and moves towards smaller angles, reaching its maximum width for a center-of-mass collision energy of 860 eV. As energy is increased beyond this, the angular distribution becomes narrower again. We know from measurements of the kinetic energies of the ions that their velocity is about 85% of the initial projectile beam velocity. With the help of the Newton diagram in the lower part of Fig. 13, we can thus estimate the amount of energy converted to internal excitation of the projectile and target for projectiles scattered at an angle corresponding to the maximum in the measured distributions. For all collision energies investigated, this works out as being close to 60% of the center-of-mass energy. Knowing the internal energy of the projectile (estimated as one-half of the total inelasticity, i.e., 30% of the center-of-mass energy plus the initial 25 eV internal energy of the projectile ion) and the average fragment size (Fig. 5), it is possible to estimate the width of the angular distribution using the simple procedure discussed above for the fusion product. In this case we consider the energy-temperature plot for $C_{60}{}^{+}$ shown in Fig. 14 to estimate the temperature. We assume that the projectile ions are first scattered inelastically and then subsequently undergo statistical fragmentation. The estimated widths are in very good qualitative agreement with the measurements. They increase from $\pm 2°$ to $\pm 5°$ on increasing the collision energy from 132 to 500 eV. For the two intermediate energies (750 and 860 eV) where one still has some fullerenelike fragments but in the low mass range for fullerenes around $n=30$, we estimate angular distributions of about $\pm 7°$. Going to still higher collision energies, the fragment mass spectrum consists of only small fragment ions (where we consider only two steps, as discussed above, a multifragmentation followed by an evaporative cooling step) and the estimated angular distribution decreases again to about $\pm 5°$.

V. CONCLUSION

We have reported detailed measurements of the mass and angular distribution of the positive ions produced in fullerene-fullerene collisions over a center-of-mass collision energy range of 115–1400 eV. Both products from completely inelastic fusion reactions and from inelastically scattered projectile ions are detected. The results are consistent with a strongly statistical fragmentation of the highly excited collision product. Support is given for an earlier suggestion of the onset of a ‘‘phase transition’’ at a collision energy of about 130 eV leading to a change in fragmentation mechanism.

ACKNOWLEDGMENTS

The authors would like to thank Dr. F. Rohmund for helpful discussions. Financial support from the Swedish Natural Sciences Research Council (NFR) is gratefully acknowledged.

---

[1] R. Schmidt, G. Seifert, and H.O. Lutz, *Nuclear Heavy-Ion and Atomic Cluster-Cluster Collisions* (Springer-Verlag, Heidelberg, Germany, 1992), p. 128.
[2] F. Rohmund, A.V. Glotov, K. Hansen, and E.E.B. Campbell, J. Phys. B **29**, 5143 (1996).
[3] O. Knospe, A.V. Glotov, G. Seifert, and R. Schmidt, J. Phys. B **29**, 5163 (1996).
[4] E.E.B. Campbell, A.V. Glotov, and F. Rohmund, in *Proceedings of the Les Houches Workshop on Nuclear Matter in Different Phases and Transitions*, edited by M. Ploszajczak (Kluwer Academic, Dordrecht, 1998), p. 493.
[5] B. Farizon, M. Farizon, and M.J. Gaillard, Int. J. Mass. Spectrom. **192**, 259 (1999).
[6] B. Farizon, M. Farizon, M.J. Gaillard, F. Gobet, C. Guillermier, M. Carre, J.P. Buch, P. Sheier, and T.D. Märk, Eur. Phys. J. D **5**, 5 (1999).
[7] *Heavy Ion Collisions*, edited by R. Bock (North Holland, Amsterdam, 1990).
[8] M.S. Dresselhaus, G. Dresselhaus, and P.C. Eklund, *Science of Fullerenes and Carbon Nanotubes* (Academic, New York, 1996).
[9] E.E.B. Campbell, V. Schyja, R. Ehlich, and I.V. Hertel, Phys. Rev. Lett. **70**, 263 (1993).
[10] F. Rohmund, E.E.B. Campbell, O. Knospe, G. Seifert, and R. Schmidt, Phys. Rev. Lett. **76**, 3289 (1996).
[11] E.E.B. Campbell, F. Rohmund, and A.V. Glotov, Nuovo Cimento A **110**, 1191 (1997).
[12] A. Itoh *et al.*, Nucl. Instrum. Methods Phys. Res. B **129**, 363 (1997).
[13] O. Knospe and R. Schmidt, in *Theory of Atomic and Molecular Clusters*, edited by J. Jellinek, Springer Series on Mesoscopic Phenomenon (Springer, Heidelberg, 1997).
[14] G. Seifert and R. Schmidt, New J. Chem. **16**, 1145 (1992).
[15] R. Schmidt, J. Schulte, O. Knospe, and G. Seifert, Phys. Lett. A **19**, 101 (1994).
[16] Y. Xia, Y. Xing, C. Tan, and L. Mei, Phys. Rev. B **53**, 13 871 (1996).
[17] Y. Xia, Y. Mu, Y. Xing, C. Tan, and L. Mei, Phys. Rev. B **56**, 4979 (1997).
[18] J. Schulte, O. Knospe, G. Seifert, and R. Schmidt, Phys. Lett. A **198**, 51 (1995).
[19] J. Schulte, Phys. Rev. B **51**, 3331 (1995).
[20] J. Schulte, Int. J. Mass Spectrom. Ion Processes **145**, 203 (1995).
[21] H. Shen, P. Hvelplund, D. Mathur, A. Barany, H. Cederquist, N. Selberg, and D.C. Lorents, Phys. Rev. A **52**, 3847 (1995).
[22] D.L. Strout, R.L. Murry, C. Xu, W.C. Eckhoff, G.K. Odom, and G.E. Scuseria, Chem. Phys. Lett. **214**, 576 (1993).
[23] D.H. Robertson, D.W. Brenner, and C.T. White, J. Phys. Chem. **99**, 15 721 (1995).
[24] X. Long, R.L. Graham, C. Lee, and S. Smithline, J. Chem. Phys. **100**, 7223 (1994).
[25] B.L. Zhang, C.Z. Wang, C.T. Chan, and K.M. Ho, J. Phys. Chem. **97**, 3134 (1993).
[26] F. Rohmund and E.E.B. Campbell, Chem. Phys. Lett. **254**, 237 (1995).
[27] F. Rohmund and E.E.B. Campbell, Z. Phys. D: At., Mol. Clusters **40**, 399 (1997).
[28] F. Rohmund and E.E.B. Campbell, J. Phys. B **30**, 5293 (1997).
[29] P. Hvelplund, L.H. Andersen, C. Brink, D.H. Yu, D.C. Lorents, and R. Ruoff, Z. Phys. D: At., Mol. Clusters **30**, 323 (1994).
[30] A.V. Glotov and E.E.B. Campbell, Chem. Phys. Lett. (to be published).
[31] E.E.B. Campbell, T. Raz, and E.D. Levine, Chem. Phys. Lett. **253**, 261 (1996).
[32] G. Seifert, K. Vietze, and R. Schmidt, J. Phys. B **29**, 5183 (1996).